

Easy-plane ferromagnetism in single-crystal ErB_2 at low temperatures

C. Resch,^{1,*} G. Benka,¹ A. Bauer,^{1,2} and C. Pfleiderer^{1,2,3,4}

¹*School of Natural Sciences, Technical University of Munich, D-85748 Garching, Germany*

²*Zentrum für QuantumEngineering (ZQE), Technical University of Munich, D-85748 Garching, Germany*

³*Munich Center for Quantum Science and Technology (MCQST),
Technical University of Munich, D-85748 Garching, Germany*

⁴*Heinz Maier-Leibnitz Zentrum (MLZ), Technical University of Munich, D-85748 Garching, Germany*

(Dated: April 30, 2025)

We report a study of single crystals of the hexagonal rare-earth diboride ErB_2 prepared by means of the self-adjusted flux travelling-solvent floating-zone technique. Measurements of the magnetization, ac susceptibility, specific heat, and electrical resistivity consistently establish ferromagnetic order of the Er^{3+} moments below a second-order phase transition at $T_c = 14$ K and a very strong easy-plane anisotropy. Curie–Weiss fits of the ac susceptibility are characteristic of ferromagnetic coupling within the easy hexagonal basal plane, and antiferromagnetic coupling along $\langle 001 \rangle$. Under magnetic field within the basal plane the magnetization is reminiscent of a soft ferromagnet that is polarized in fields above a few tenths of a Tesla, vanishing hysteresis and negligible in-plane anisotropy. Under field along $\langle 001 \rangle$, typical hard-axis behavior is observed with the magnetization increasing only weakly up to a spin-flip transition at $\mu_0 H_c = 12$ T. The easy-plane anisotropy emerges below a crossover temperature $T_x \approx 50$ K, i.e. a broad paramagnetic temperature range above T_c is governed by strongly anisotropic magnetic fluctuations.

PACS numbers:

I. MOTIVATION

The C32 diborides, MB_2 , crystallize in a bilayer hexagonal structure, space group $P6/mmm$. Depending on the element M , a wide range of electronic and magnetic properties may be observed,^{1–12} with superconductivity in MgB_2 representing the perhaps most prominent example^{13–16}. In diborides based on rare-earth elements, at low temperatures typically magnetic order emerges with localized f-electron moments in the presence of strong magnetocrystalline anisotropy and geometric frustration^{17–21}. In this context, scenarios such as quantum criticality under transversal field tuning^{22–24}, large anomalous Hall effects in noncollinear magnets^{25–27}, or solitonic excitations in Ising-like systems^{28,29} may be realized in a relatively simple crystallographic environment. However, due to high melting temperatures, high vapor pressures, and peritectic metallurgical reactions, the preparation of rare-earth diborides can be challenging and studies of single-crystals are scarce.

ErB_2 is a typical representative of the class of rare-earth diborides. Early studies of polycrystalline ErB_2 reported magnetic order below ~ 16 K that was attributed to ferromagnetic interactions due to a positive Curie–Weiss temperature¹⁷. A kink in the resistivity³⁰, consistent with an anomaly in the specific heat³¹, was attributed to an onset of magnetic order below ~ 14 K, while the lattice constant c was reported to increase below about 100 K³². The polycrystalline sample for these studies were prepared by means of high-pressure synthesis followed by annealing and contained several percent of impurity phases³³. Studies of single-crystals were so far restricted to thin platelets of $1 \times 1 \times 0.01$ mm³³⁴. Recent studies of polycrystalline and single-crystal ErB_2 suggest

that magnetic order is stabilized under pressures up to 5.6 GPa.^{35,36} Consequently, no details of the nature of the magnetic order, the magnetic field dependence, and the magnetocrystalline anisotropy had been reported.

We report an investigation of the low-temperature properties of large single crystals of ErB_2 . The single-crystal ingots were prepared by means of the self-adjusted flux travelling-solvent floating-zone approach, as reported in Refs. 37–39. Magnetic order of the Er^{3+} moments below a second-order phase transition at $T_c = 14$ K is consistently observed in the magnetization, ac susceptibility, specific heat, and electrical resistivity. Curie–Weiss fits of the ac susceptibility suggest that the moments are coupled ferromagnetically in the hexagonal basal plane and antiferromagnetically along the $\langle 001 \rangle$ axis. The magnetocrystalline anisotropy is strong and may be described by a magnetic hard $\langle 001 \rangle$ axis and an easy hexagonal basal plane with negligible in-plane anisotropy. The paramagnetic state exhibits strongly anisotropic magnetic fluctuations up to a crossover temperature $T_x \approx 50$ K well above T_c .

For magnetic fields applied within the basal plane, the field dependence of the magnetization is reminiscent of a soft ferromagnet with vanishing hysteresis. For fields along $\langle 001 \rangle$, the magnetization at low temperatures shows typical hard-axis behavior with a spin-flip transition at $\mu_0 H_c = 12$ T. Combining measurements of the magnetization, the ac susceptibility, and the electrical resistivity for a large number of temperatures and fields, magnetic phase diagrams are inferred for magnetic fields applied along $\langle 100 \rangle$, $\langle 210 \rangle$, and $\langle 001 \rangle$.

Our paper is organized as follow. In Sec. II the experimental methods are described. The presentation of the experimental results starts with the temperature dependence of the ac susceptibility and the specific heat in zero

magnetic field in Secs. III A and III B, respectively. This is followed by the magnetic field dependence of the magnetization, addressing also demagnetization effects, and the temperature dependence of the magnetization and the ac susceptibility at high magnetic fields in Sec. III C. In Sec. III D, the temperature dependence of the electrical resistivity is reported, followed by the magnetic phase diagrams in Sec. III E. Our results are discussed briefly and summarized in Sec. IV.

II. EXPERIMENTAL METHODS

As reported in Ref. 37, a large single-crystal ingot of ErB_2 , forming in a weakly peritectic reaction, was grown by means of the self-adjusted flux travelling-solvent floating-zone approach. After a thorough metallurgical characterization, establishing phase-pure single-crystal material, the ingot was oriented by means of x-ray Laue diffraction and samples were cut using a wire saw. Four samples were used in the present study: (i) a cuboid of $2.5 \times 1.4 \times 1 \text{ mm}^3$ oriented along $\langle 001 \rangle \times \langle 100 \rangle \times \langle 210 \rangle$, (ii) a cube with an edge length of 0.5 mm oriented the same way, (iii) a platelet of $2 \times 1 \times 0.18 \text{ mm}^3$ oriented along $\langle 001 \rangle \times \langle 210 \rangle \times \langle 100 \rangle$, and (iv) a platelet of $1.2 \times 1 \times 0.16 \text{ mm}^3$ oriented along $\langle 100 \rangle \times \langle 210 \rangle \times \langle 001 \rangle$.

Measurements of the magnetization, the ac susceptibility, and the specific heat were carried out in Quantum Design physical property measurement system at temperatures down to 2 K under magnetic fields up to 14 T. The magnetization was measured with the standard extraction technique of the ACMS-II option. The ac susceptibility was measured with an excitation frequency of 911 Hz at an excitation amplitude of 1 mT. The specific heat was measured using a quasiadiabatic large heat pulse technique, where typical pulses had a size of 30% of the temperature at the start of the pulse⁴⁰. The Specific heat data as well as the ac susceptibility in finite fields were measured on sample (i). Due to the pronounced magnetocrystalline anisotropy of ErB_2 , samples can exert considerable magnetic torque under applied magnetic field, requiring the use of the smaller sample (ii) for the magnetization measurements as a function of field applied along the hard $\langle 001 \rangle$ axis. For the sake of consistency, the ac susceptibility data for zero field and the magnetization data for finite fields within the easy basal plane were measured on the same sample (ii).

Measurements of the electrical resistivity were carried out in conventional superconducting magnet systems equipped with a variable temperature insert. For these measurements, samples (iii) and (iv) were contacted by means of $\text{Al}_{99}\text{Si}_1$ wires. The electrical resistivity was measured using low-noise impedance-matching transformers (Signal Recovery Model 1900), digital lock-in amplifiers (Stanford Research SR830), and a precision current source (Keithley 6221). Data were recorded at an excitation frequency of 22.08 Hz and an excitation current of several mA. The magnetic field was applied

perpendicular to the current direction. For magnetic fields applied along the hard magnetic axis, notably sample (iv), the sample was attached using Stycast 2850 FT epoxy. For all resistivity samples studied, a low residual resistivity of a few $\mu\Omega\text{cm}$ was observed characteristic of excellent sample quality.

If not stated otherwise, data were recorded after zero-field cooling. Measurements of the magnetization as a function of field at low temperatures were carried out in terms of hysteresis loops including magnetic virgin curves. At the level of the resolution of our data, no hysteresis was observed. For clarity, the magnetization data in Figs. 3 and 4 are shown as a function of decreasing field only.

In magnetic materials, demagnetization effects may lead to discrepancies between applied and internal magnetic fields in both field strength and orientation. Approximating the samples as rectangular prisms⁴¹, the demagnetization factors N of the samples used in our study were $N_i^{001} = 0.19$, $N_i^{100} = 0.34$, $N_i^{210} = 0.47$, $N_{ii} = 0.33$, $N_{iii}^{100} = 0.76$, and $N_{iv}^{001} = 0.75$, where the subscript refers to the sample number. The internal magnetic field values H_{int} were calculated from the applied field H_{ext} using the measured magnetization $M(H_{\text{ext}})$ using $H_{\text{int}} = H_{\text{ext}} - NM(H_{\text{ext}})$. As the magnetization changes with temperature, data as a function of temperature at constant applied field do not correspond directly to data at constant internal field. To avoid ambiguities, data are therefore shown as a function of applied field, if not stated otherwise. In order to combine data measured on samples with different geometry into a single magnetic phase diagram, for each data point demagnetization effects are considered separately for the given temperature and field value, cf. also Ref. 42. Furthermore, in measurements of the ac susceptibility, demagnetization effects also modify the absolute value via the excitation field. The internal ac susceptibility, $\chi_{\text{ac}}^{\text{int}}$, may be calculated from $\chi_{\text{ac}}^{\text{ext}}$, using $\chi_{\text{ac}}^{\text{int}} = \chi_{\text{ac}}^{\text{ext}} / (1 - N\chi_{\text{ac}}^{\text{ext}})$, as discussed below.

III. EXPERIMENTAL RESULTS

A. AC Susceptibility in Zero Field

The presentation of our experimental results starts with the temperature dependence of the ac susceptibility at zero field for excitation fields parallel to the major crystallographic axes, shown in Fig. 1(a). As a function of decreasing temperature the susceptibility exhibits a Curie–Weiss dependence. In the basal plane, this behavior continues until a kink at $T_c = 14 \text{ K}$ is followed by a decrease of the susceptibility, characteristic of the onset of long-range magnetic order. Data for excitations along $\langle 100 \rangle$ and $\langle 210 \rangle$ essentially track each other, characteristic of a vanishingly small in-plane anisotropy. For $\langle 001 \rangle$, the absolute value of the susceptibility is smaller, characteristic of a hard magnetic axis, and the temperature dependence deviates from the Curie–Weiss-like behavior

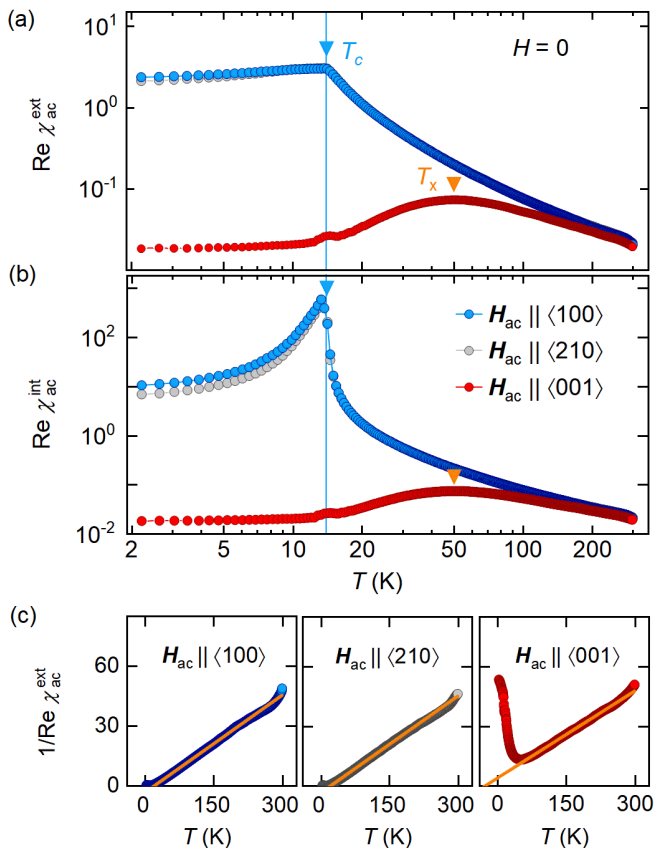


FIG. 1: Real part of the ac susceptibility as a function of temperature in zero magnetic field, $H = 0$. Data are shown for ac excitation fields applied along the major crystallographic axes $\langle 100 \rangle$ (blue symbols), $\langle 210 \rangle$ (gray symbols), and $\langle 001 \rangle$ (red symbols). (a) Measured susceptibility on a double-logarithmic scale. (b) Susceptibility on a double-logarithmic scale when correcting for the demagnetization effects in the ac excitation field. (c) Inverse of the measured ac susceptibility. Orange lines are linear Curie-Weiss fits.

observed at the highest temperatures studied. Instead, a shallow maximum may be observed at $T_x \approx 50$ K. Such a maximum is characteristic of a crossover that may be attributed to the emergence of strong magnetic anisotropy at low temperatures. Below T_x , the magnetic anisotropy prevails over thermal fluctuations, effectively reducing the dimensionality of the magnetic fluctuation spectrum by restricting fluctuations to the hexagonal basal plane. At T_c , a weak cusp is observed that may reflect a small misalignment of the ac excitation field with respect to the $\langle 001 \rangle$ axis of the order of 1 deg, resulting in a tiny in-plane component of the excitation field.

When calculating the ac susceptibility with respect to the internal magnetic field scale by taking into account the demagnetization effects, qualitatively similar behavior is observed, as shown in Fig. 1(b). However, the absolute value of the susceptibility increases, in particular for temperatures around T_c and below. High values of up to 600 are reached, reminiscent of soft ferromagnets.

For further quantitative analysis, the inverse of the measured ac susceptibility in the paramagnetic regime is fitted linear Curie-Weiss dependence, as shown in Fig. 1(c). In the paramagnetic state, the susceptibility is comparably small and demagnetization effects are mostly negligible. For excitation fields within the basal plane, a linear regression between 50 K and 250 K yields fluctuating magnetic moments of $\mu_{\text{eff}}^{(100)} = 9.13 \mu_B \text{ f.u.}^{-1}$ and $\mu_{\text{eff}}^{(210)} = 9.15 \mu_B \text{ f.u.}^{-1}$ as well as Curie-Weiss temperatures $\Theta_{\text{CW}}^{(100)} = \Theta_{\text{CW}}^{(210)} = 19.0$ K. For excitation fields parallel to $\langle 001 \rangle$, a linear regression between 100 K and 250 K yields $\mu_{\text{eff}}^{(001)} = 9.64 \mu_B \text{ f.u.}^{-1}$ and $\Theta_{\text{CW}}^{(001)} = -29.8$ K. The fluctuating moments are close to the free-ion value of Er^{3+} , $\mu_{\text{eff}} = 9.58 \mu_B \text{ f.u.}^{-1}$, consistent with magnetism that is carried by the 4f electrons on the rare-earth sites. The positive and the negative sign of Θ_{CW} in the basal plane and perpendicular to the basal plane, respectively, suggest that the interactions are ferromagnetic within the basal plane and antiferromagnetic perpendicular to it.

Antiferromagnetic interactions in an hexagonal environments as well as competing interactions in general may give rise to frustration effects. The ratio $f = -\Theta_{\text{CW}}/T_c$ is commonly used to quantify the suppression of long-range magnetic order due to frustration, where values exceeding ten are considered a hallmark of strongly frustrated systems⁴³. In ErB_2 , a value of $f_{\langle 001 \rangle} = 2.1$ is observed for the c-axis, characteristic of a system in which very weak geometrical frustration may be present.

B. Specific Heat

The specific heat as a function of temperature is shown in Fig. 2(a). At low temperatures, a lambda anomaly is observed at T_c , characteristic of a second-order phase transition consistent with the susceptibility. At high temperatures, the specific heat slowly approaches the Dulong-Petit value of $9R = 74.8 \text{ J mol}^{-1} \text{ K}^{-1}$. To account for nonmagnetic contributions, the specific heat of the isostructural C32 compound LuB_2 was measured on a polycrystal prepared by means of arc melting⁴⁴. At high temperatures, the specific heat of nonmagnetic LuB_2 essentially tracks that of ErB_2 at slightly smaller absolute values. Below about 100 K, ErB_2 exhibits additional contributions that are absent in its nonmagnetic counterpart. These contributions may be attributed to magnetic fluctuations that emerge well above the onset of long-range magnetic order at T_c . They relate to the crossover at T_x observed in the ac susceptibility.

For comparison, a phonon contribution is shown as calculated by means of the Debye model (solid line). The Debye temperature $\Theta_D = 735$ K was chosen such that the calculated phonon contribution approaches the data at high temperatures while staying at smaller absolute values. In particular at intermediate temperatures, namely

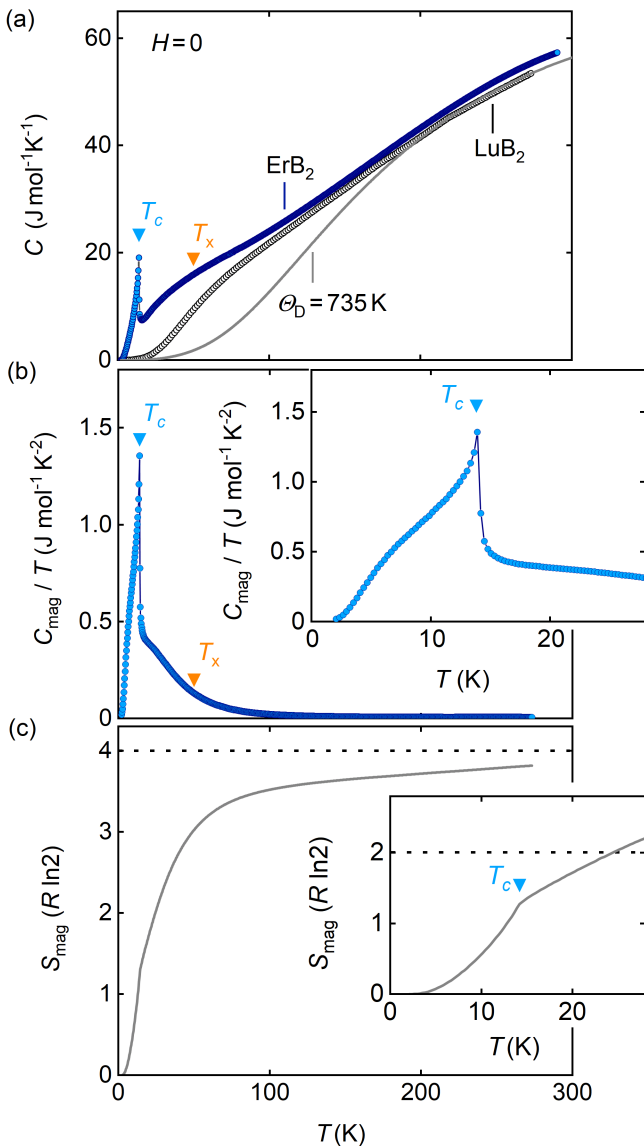


FIG. 2: Specific heat of ErB_2 as a function of temperature in zero magnetic field. For comparison, data of nonmagnetic LuB_2 (open symbols) and a Debye model with a Debye temperature $\Theta_D = 735$ K (solid line) are shown. (b) Magnetic contribution to the specific heat divided by temperature after subtracting the specific heat of LuB_2 as nonmagnetic contribution. Inset: Enlarged view at low temperatures. (c) Magnetic contribution to the entropy, approaching $4 \ln 2$ at high temperatures. Inset: Enlarged view at low temperatures.

between 30 K and 180 K, a large discrepancy is observed between the Debye model and the measured specific heats of both LuB_2 and ErB_2 . Akin to other diborides^{12,21,45}, discrepancies with nonmagnetic LuB_2 may be attributed to the reduced effective dimensionality associated with the layered crystal structure, beyond the assumptions of the Debye model⁴⁹.

Using the specific heat of LuB_2 to subtract nonmagnetic signal contributions, the magnetic part of the spe-

cific heat divided by temperature is shown in Fig. 2(b). This contribution is dominated by the lambda anomaly at T_c . Below T_c , an additional hump may be observed around 8 K, reminiscent to the behavior observed in the itinerant antiferromagnet CrB_2 ¹². A reliable extrapolation of the specific heat to zero temperature is not possible due to the large slope of C/T at the lowest temperatures studied. However, the value of $20 \text{ mJ mol}^{-1} \text{K}^{-2}$ at 2 K implies a Sommerfeld coefficient of the order of a few $\text{mJ mol}^{-1} \text{K}^{-2}$ in ErB_2 , characteristic of a material with comparatively weak electronic correlations. At temperatures above T_c , sizeable magnetic contributions are observed as associated with the crossover phenomenon at T_x , consistent with the ac susceptibility.

Numerically integrating the specific heat divided by temperatures yields the magnetic contribution to the entropy shown in Figs. 2(c). For Er^{3+} , Hund's rules imply $J = 15/2$ and a magnetic contribution to the entropy $S_{\text{mag}} = 4R \ln 2$ at high temperatures. The magnetic phase transition at T_c is associated with a clear kink releasing $1.3R \ln 2$ at T_c . This indicates that the anisotropic magnetic fluctuations in the paramagnetic regime above T_c carry large parts of the magnetic entropy. Up to room temperature, the magnetic contribution to the entropy approaches $4R \ln 2$, in excellent agreement with magnetism arising due to Er^{3+} moments.

C. Magnetization and AC Susceptibility

The evolution of the magnetic properties as a function of field is illustrated by means of the field dependence of the magnetization. For magnetic field applied within the basal plane, shown in Fig. 3(a), the magnetization exhibits an S-shape with pronounced changes of slope around ± 0.8 T characteristic of the onset of the field-polarized state at high fields. Up to 14 T, the highest field studied, the slope remains finite with the magnetization reaching $7.5 \mu_B/\text{f.u.}$. This value is smaller than the free-ion value of $9.0 \mu_B \text{ f.u.}^{-1}$ of Er^{3+} . In combination with the lack of saturation, such discrepancy typically is attributed to itinerant magnetism, suggesting that the 4f electrons of Er^{3+} in fact may be hybridized with d electrons at the Fermi level. Data for field parallel to $\langle 100 \rangle$ and $\langle 210 \rangle$ essentially track each other, characteristic of vanishing in-plane anisotropy. No hysteresis was observed at the level of the resolution of our study.

When taking into account demagnetization effects, shown in Fig. 3(b), the slope around zero field becomes very steep and the onset of the field-polarized regime shifts to much smaller field values. This behavior is strongly reminiscent of a soft ferromagnetic material in which magnetic domains reorient or change population under small magnetic fields.

For magnetic field parallel to $\langle 001 \rangle$, shown in Fig. 1(c), the magnetization at small fields increases only weakly, staying below $1 \mu_B \text{ f.u.}^{-1}$ up to 11 T. Around 12 T a pronounced increase is observed, characteristic of a spin-

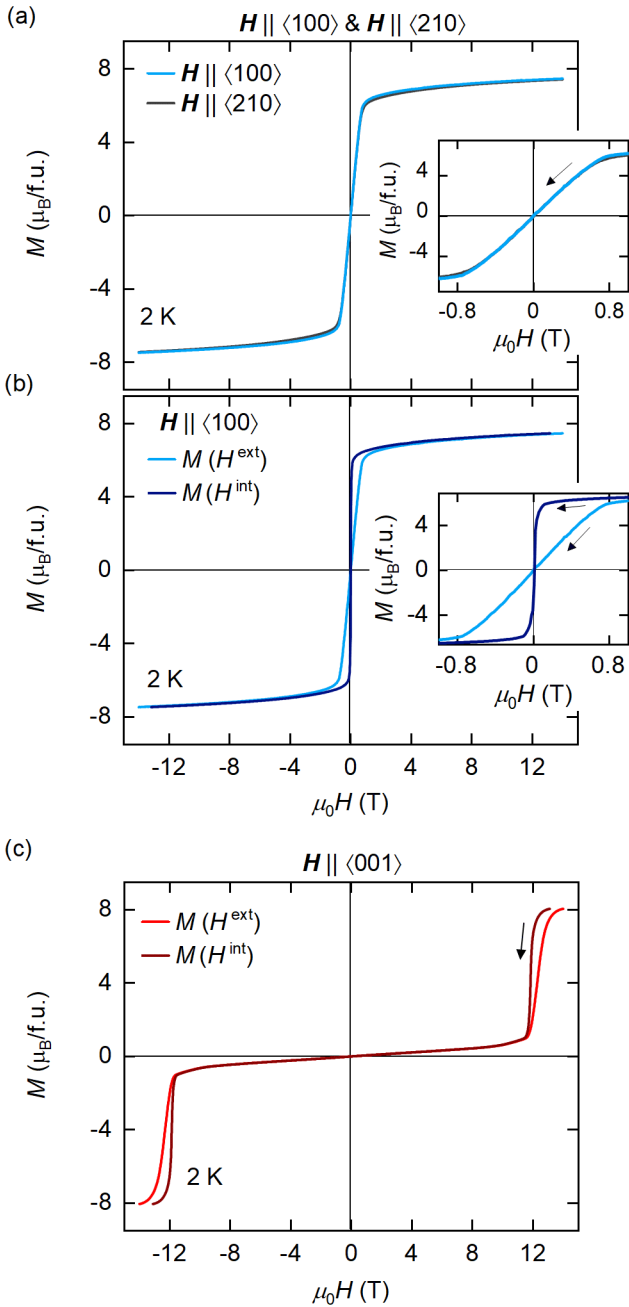


FIG. 3: Magnetization as a function of field at low temperature. (a) Magnetization for field along $\langle 100 \rangle$ and $\langle 210 \rangle$. Data are shown for decreasing field (black arrow). (b) Magnetization for field along $\langle 100 \rangle$ as a function of applied and internal field. Insets: Enlarged view of the low-field behavior. (c) Magnetization for field along $\langle 001 \rangle$ as a function of applied and internal field.

flip transition into the field-polarized state. The slope at high fields decreases, but remains finite with the magnetization reaching $8.1 \mu_B f.u.^{-1}$ at 14 T below the free-ion value of Er^{3+} . Taking into account demagnetization effects, the spin-flip transition is shifted to slightly smaller internal field values and the increase of the magnetization

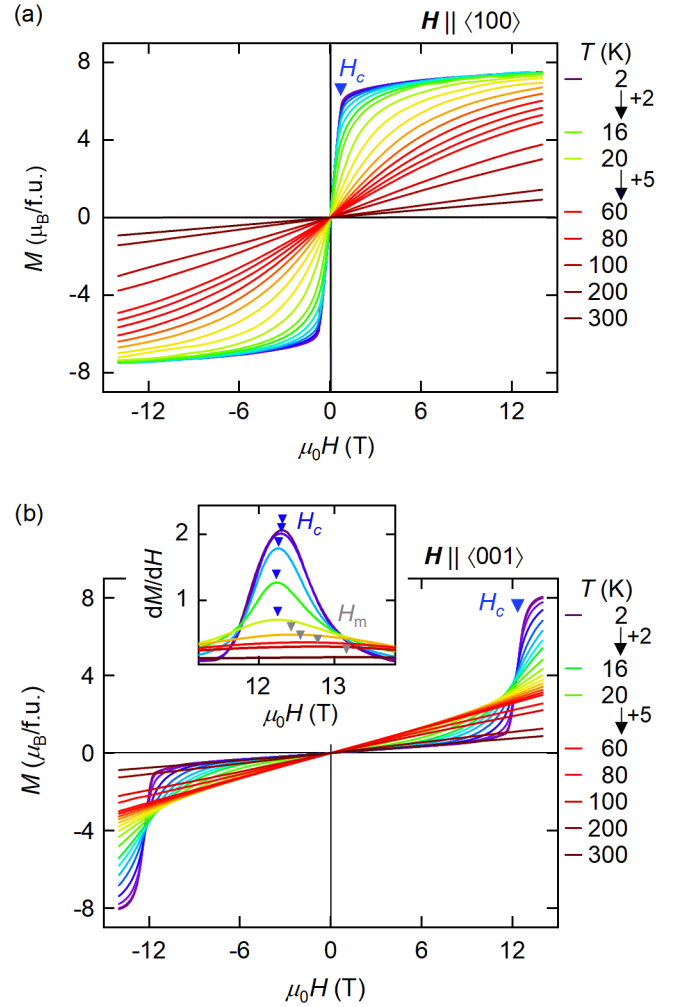


FIG. 4: Magnetization as a function of field for different temperatures. (a) Magnetization for field along the magnetic easy $\langle 100 \rangle$ axis. (b) Magnetization for field along the magnetic hard $\langle 001 \rangle$ axis. Inset: Differential susceptibility, dM/dH , around the spin-flip transition.

associated with the transition becomes very steep.

Taken together, the magnetization for fields applied along the major crystallographic axes establish ErB_2 as a ferromagnetic material that is dominated by strong magnetic anisotropies, where $\langle 001 \rangle$ is the hard magnetic axis and the basal plane is magnetically easy with vanishingly small in-plane anisotropy.

Under increasing temperature, the magnetization for field applied along the magnetic easy $\langle 100 \rangle$ axis remains qualitatively unchanged, as shown in Fig. 4(a). The absolute value decreases monotonically as the change of slope associated with the onset of the field-polarized state at high fields becomes increasingly rounded, in particular for temperatures exceeding T_c . The characteristic field $H_c^{(100)}$ may be tracked in terms of a point of inflection in the differential susceptibility (not shown). At temperatures well above T_c , the magnetization curve exhibits the

shape of the Brillouin function, characteristic of paramagnetic behavior.

For field along the $\langle 001 \rangle$ hard magnetic axis shown in Fig. 4(b), the jump-like increase of the magnetization around 12 T represents the most prominent feature, characteristic of a spin-flip into the field-polarized state. Under increasing temperature, this jump broadens and decreases. The transition field of the spin-flip, $H_c^{(001)}$, may be inferred from the point of inflection in the magnetization, which may be tracked conveniently in the differential susceptibility, dM/dH shown in the inset of Fig. 4(b). Below T_c , a maximum is observed in dM/dH that becomes less pronounced, where the field value does not change for increasing temperature. Above T_c , a shallow maximum at H_m may be resolved at least up to 30 K, which slowly shifts to larger field values. This maximum is associated with the crossover into the field-polarized state at high fields.

The magnetization as a function of the temperature provides complementary information to the magnetic field dependence. For field along the magnetic easy $\langle 100 \rangle$ axis shown in Fig. 5(a), the magnetization at the lowest fields essentially corresponds to the ac susceptibility. As a function of decreasing temperature, a Curie–Weiss dependence of the magnetization is followed by a kink at $T_c = 14$ K and becomes essentially constant below T_c . Under increasing field, the absolute value of the magnetization increases, the kink at T_c gets rounded and shifts to smaller temperatures. At high fields, the magnetization increases smoothly and levels off at values of up to $7.5 \mu_B/\text{f.u.}$ at low temperatures. As emphasized above, internal field values at small fields are significantly smaller than the applied field values and, perhaps more importantly, changes as a function of temperature as combined with the strength of the demagnetization effects. Therefore, the kink at T_c under finite magnetic field may be attributed to domain reorientation or repopulation of multi-domain ferromagnetic order.

For field along the $\langle 001 \rangle$ hard magnetic axis, the temperature dependence of the magnetization is shown in Fig. 5(b) and Fig. 5(c) for high and low fields, respectively. At the lowest fields, the magnetization resembles the ac susceptibility, namely a shallow maximum is observed around $T_x = 50$ K, followed by a weak cusp at T_c that may be associated with a fortuitous small in-plane component of the applied magnetic field. Under increasing field, the absolute value of the magnetization increases. The temperature of the cusp remains essentially constant and vanishes for fields exceeding ~ 2 T. The maximum at T_x becomes more pronounced and shifts to lower temperatures, vanishing above 12 T. At highest fields, the magnetization exhibits high values at low temperatures, reaching more than $8 \mu_B/\text{f.u.}$, characteristic of the field-polarized regime. These values are in excellent agreement with the data as a function of field.

While the ac susceptibility at the lowest fields (not shown) mirrors the evolution of the magnetization under field, it exhibits an additional crossover at high fields. As

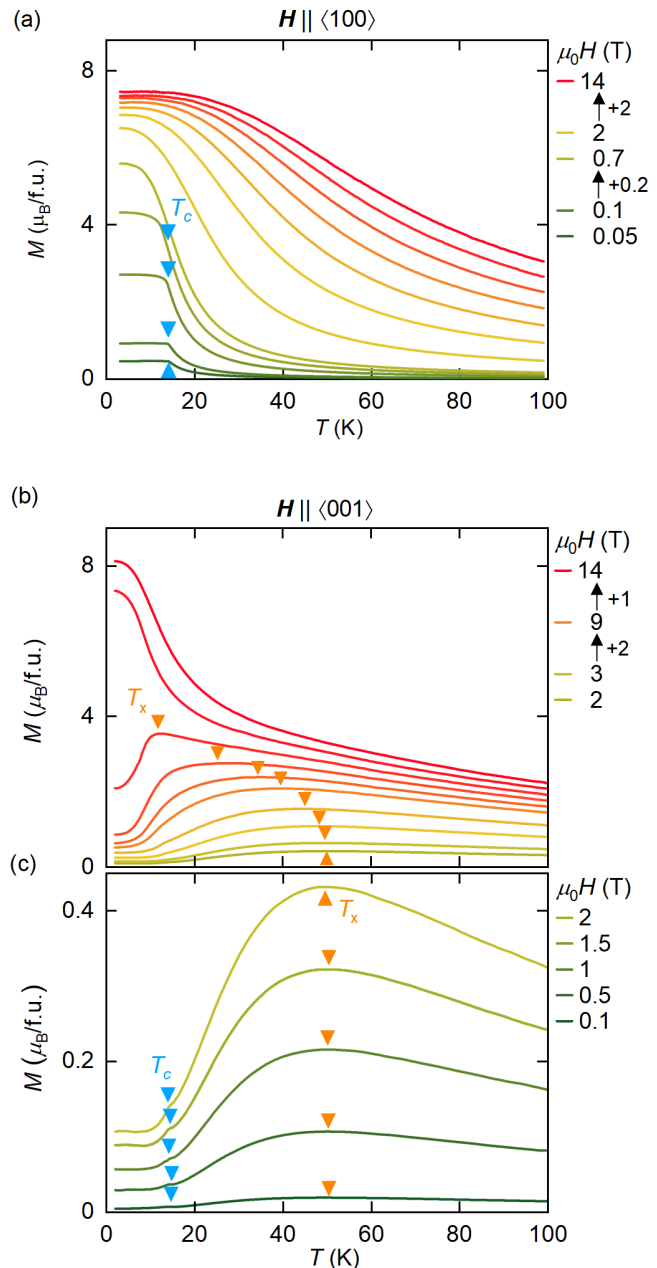


FIG. 5: Magnetization as a function of temperature for different applied magnetic fields. (a) Magnetization for field along the magnetic easy $\langle 100 \rangle$ axis. (b), (c) Magnetization for field along the magnetic hard $\langle 001 \rangle$ axis.

shown in Fig. 6(a) for field along the $\langle 100 \rangle$ easy magnetic axis, the temperature dependence of the ac susceptibility exhibits a broad maximum, denoted T_m , above the onset of ferromagnetic order at T_c . Under increasing field, the absolute value of the susceptibility decreases and the maximum shifts to higher temperatures. For field along the magnetic hard $\langle 001 \rangle$ axis, shown in Fig. 6(b), a similar maximum is observed for fields above the spin-flip transition at 12 T. These maxima mark the crossover

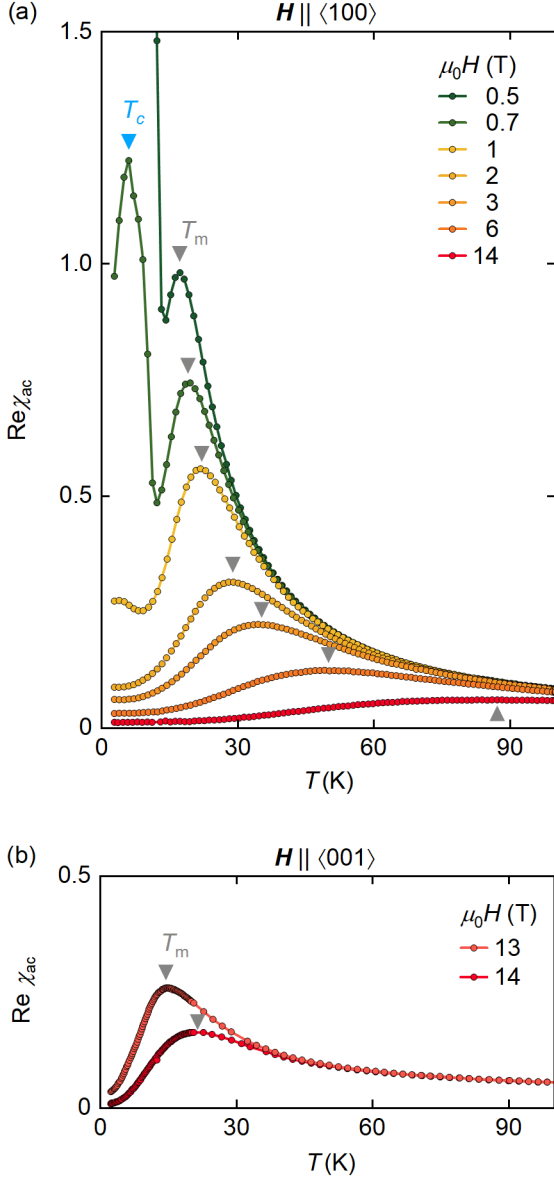


FIG. 6: AC susceptibility as a function of temperature for different applied magnetic fields. (a) Susceptibility for field along the magnetic easy $\langle 100 \rangle$ axis. (b),(c) Susceptibility for field along the magnetic hard $\langle 001 \rangle$ axis.

between the field-polarized regime at low temperatures and the paramagnetic regime at high temperatures, as reported in a wide range of magnetic materials^{46–48}.

D. Electrical Resistivity

The electrical resistivity was measured for two configurations: (i) magnetic field along an easy axis and current along the hard axis, shown in Fig. 7, and, (ii), magnetic field along the hard axis and current along an easy axis, shown in Fig. 8. As shown in Fig. 7(a), for

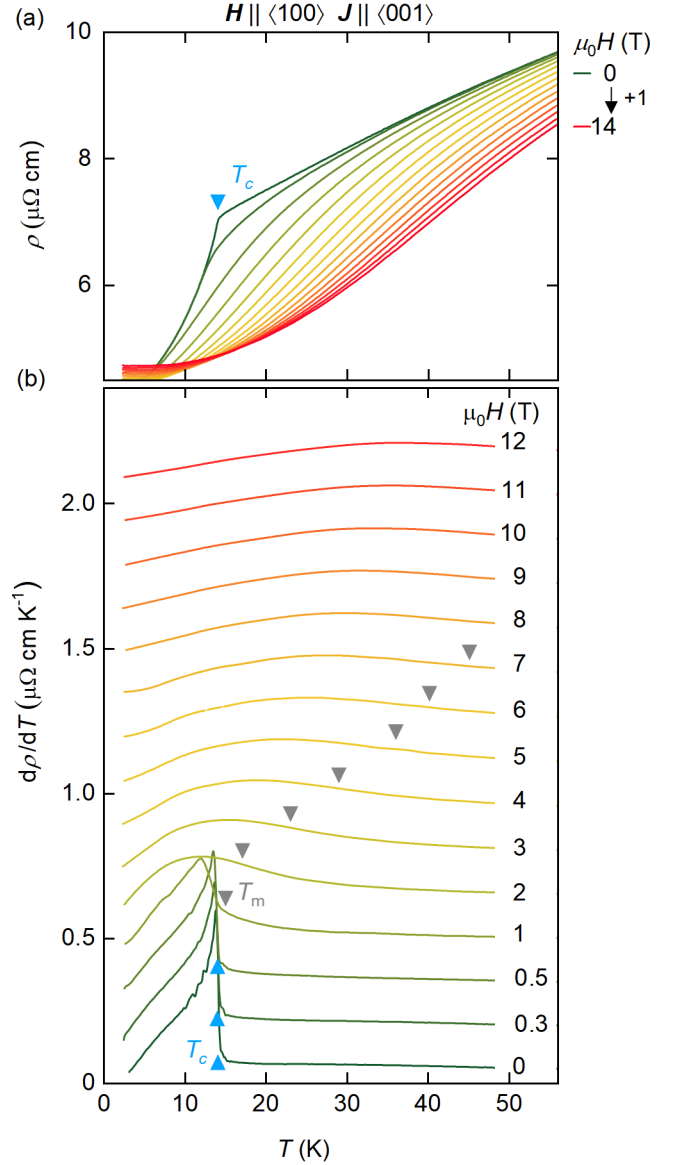


FIG. 7: Electrical resistivity as a function of temperature for magnetic field along $\langle 100 \rangle$ and current along $\langle 001 \rangle$. (a) Resistivity for different magnetic fields. (b) Derivative of the resistivity with respect to temperature for different magnetic fields.

field along $\langle 100 \rangle$ and current along $\langle 001 \rangle$ the resistivity decreases with decreasing temperature characteristic of a good a metal. A kink at T_c is followed by a pronounced decrease of the resistivity, characteristic of the onset of ferromagnetic order and a freezing out of a scattering mechanism, notably spin fluctuations. The temperature dependence of the resistivity below T_c varies as T^2 . Given the strongly anisotropy ferromagnetic state it is not possible to discriminate electron-magnon scattering from electron-electron scattering expected in a Fermi liquid. Under small magnetic fields, the resistivity at low temperatures tracks each other up to T_c , where the kink

is rounded and shifted to lower temperatures. When further increasing the applied magnetic field, the resistivity varies characteristic of a conventional magnetoresistance.

The evolution of the characteristic features under field associated with features in the magnetization, susceptibility and specific heat, may be tracked quite conveniently in the derivative of the resistivity with respect to temperature, $d\rho_{xx}/dT$, shown in Fig. 7(b). At zero field, $d\rho_{xx}/dT$ is strongly reminiscent of the electronic contribution to the specific heat divided by temperature reported above. This establishes that both quantities are dominated by the same electronic density of states at the Fermi level.

A point of inflection corresponds to the magnetic transition at T_c . Under increasing field, the asymmetric peak at T_c decreases and broadens, shifting to lower temperatures. Above 0.5 T, the pronounced peak develops into a broad maximum that shifts to higher temperatures. The point of inflection at the high-temperature side, denoted T_m , coincides with the crossover between the field-polarized regime at low temperatures and the paramagnetic regime at high temperatures. In view of the discussion of the magnetization data in Figs. 3(b) and 5(a), the kink at T_c in finite applied field may be attributed to domain reorientation processes of multi-domain ferromagnetic order.

As shown in Fig. 8(a), the resistivity for current along $\langle 100 \rangle$ in zero field resembles the resistivity for current along $\langle 001 \rangle$, including the absolute value, the pronounced kink at T_c , and the T^2 temperature dependence below T_c . For applied magnetic field along $\langle 001 \rangle$, the kink at T_c becomes rounded while staying at unchanged temperature. In general, positive magnetoresistance is observed up to 13 T when the magnetoresistance becomes negative for all but the lowest temperatures.

The derivative of the resistivity as a function of temperature, shown in Fig. 8(b), allows to track the evolution of the onset of ferromagnetic order under field more conveniently. At zero field, the data resemble the behaviour for current along $\langle 001 \rangle$ and in turn the electronic contribution to the specific heat divided by temperature. Under field, the maximum attributed to the onset of magnetic order becomes smaller, and the temperature of the point of inflection on the high-temperature side, marking T_c , remains unchanged up to 9 T. For larger fields, T_c shifts to smaller temperatures before vanishing above 14 T. When taking into account demagnetizing fields, the maximum observed at 14 T may be attributed to a crossover emerging from the spin-flip transition. Above 14 T, a shallow maximum is observed that shifts to higher temperatures with increasing field. Similar to the properties for field along $\langle 100 \rangle$, the point of inflection at the high-temperature side of this maximum may be denoted T_m and associated with the crossover between the field-polarized and the paramagnetic regime.

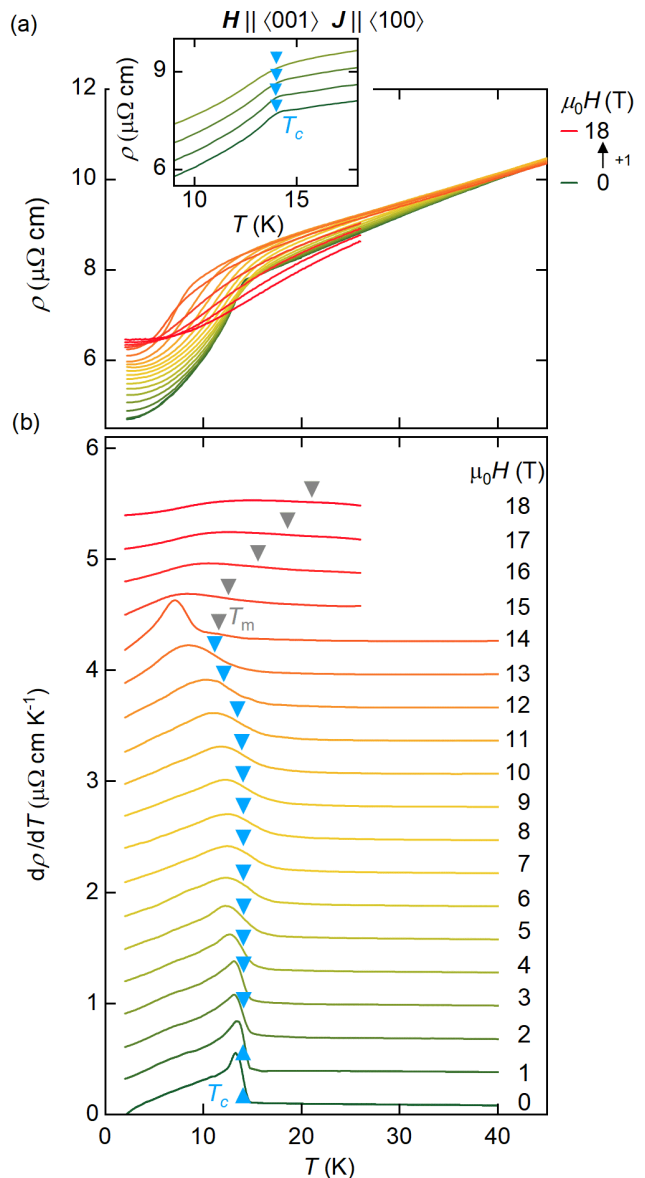


FIG. 8: Electrical resistivity as a function of temperature for magnetic field along $\langle 001 \rangle$ and current along $\langle 100 \rangle$. (a) Resistivity for different magnetic fields. Inset: Enlarged view of the behavior at small fields around T_c . (b) Derivative of the resistivity with respect to temperature for different magnetic fields.

E. Magnetic Phase Diagrams

The magnetic phase diagrams shown in Fig. 9 were inferred from the combined data reported in this paper. Magnetic field values are corrected for demagnetizing fields, allowing to combine data recorded in samples with different geometry, namely the magnetization and resistivity data. Circles, diamonds, hexagons, and stars denote data points inferred from measurements of the magnetization, the electrical resistivity, the ac susceptibility, and the specific heat, respectively. Solid and

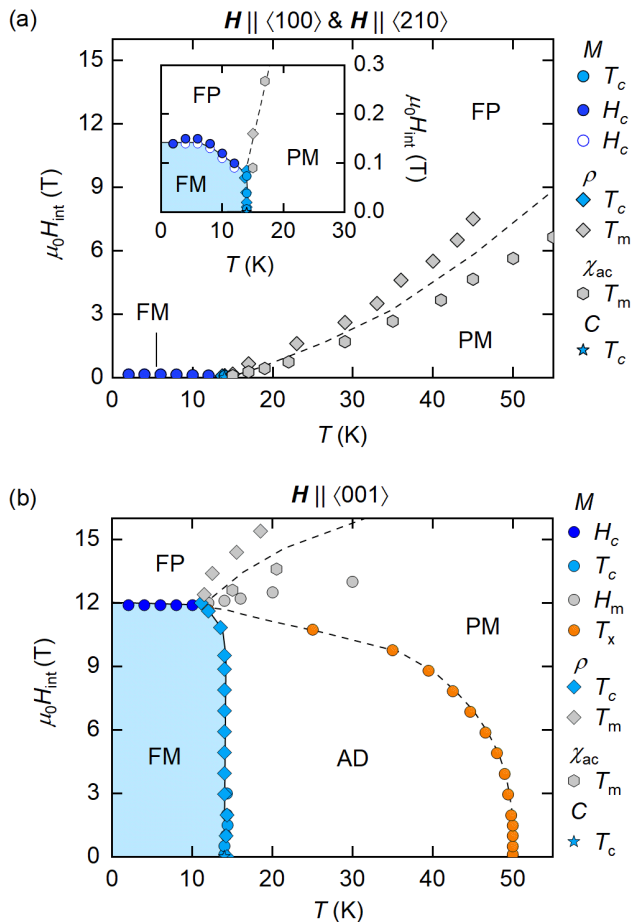


FIG. 9: Magnetic phase diagrams for magnetic fields along the major crystallographic axes. To obtain estimates for the internal field values, demagnetization effect were taken into account. (a) Diagram for field in the magnetic easy basal plane, combining data measured for field parallel to $\langle 100 \rangle$ (solid symbols) and $\langle 210 \rangle$ (open symbols). Ferromagnetic ordered (FM), paramagnetic (PM), and field-polarized (FP) regimes are distinguished. Inset: Diagram for small fields. (b) Diagram for field along the magnetic hard $\langle 001 \rangle$ axis. An anisotropy-dominated (AD) regime is observed at temperatures above the long-range ordered state.

dashed lines mark phase transitions and crossovers.

For field within the easy magnetic basal plane, shown in Fig. 9(a), the magnetic phase diagram is that of a soft ferromagnet with a transition temperature $T_c = 14$ K. Results for field parallel to $\langle 100 \rangle$ (solid symbols) and $\langle 210 \rangle$ (open symbols) highly resemble each other, consistent with vanishingly small in-plane anisotropy. As the internal field exceeds the very weak in-plane anisotropy, the behavior is characteristic of domain rearrangement processes in a material with multi-domain ferromagnetic order (FM) in which a field-polarized regime (FP) is induced. At high temperatures, a paramagnetic regime (PM) is observed.

For field parallel to the hard magnetic $\langle 001 \rangle$ axis, shown in Fig. 9(b), the properties are consistent with

ferromagnetic order up to high magnetic fields, featuring a spin-flip transition into the field-polarized state at $\mu_0 H_c^{(001)} = 12$ T. Above T_c a magnetic anisotropy-dominated paramagnetic regime (AD) may be distinguished below ~ 50 K. This regime may be described by a reduced dimensionality of the fluctuation spectrum, where the magnetic moments are essentially confined to the hexagonal basal plane. No additional signatures are observed for magnetic field within the basal plane suggestive of antiferromagnetic correlations or a more complex magnetic state beyond easy-plane ferromagnetism. At higher temperatures, the effects of the magnetic anisotropy are overcome and the magnetic moments may fluctuate in all three dimensions, characteristic of a magnetically isotropic paramagnetic regime. A crossover line, as inferred from a maximum in the magnetization, separates the anisotropy-dominated and the isotropic paramagnetic regime.

At high fields, the magnetic moments are aligned along the field direction, supporting a field-polarized regime, where the crossover towards the paramagnetic state may be tracked in various quantities. In the magnetization, the ac susceptibility, and the electrical resistivity, the crossover temperatures and fields follow the same trends, namely they increase with increasing temperature, but differ in their absolute values.

Regardless of the precise definition, this crossover as well as the crossover between the anisotropy-dominated and the paramagnetic regime both emanate from the field-induced spin-flip transition at 12 T and 12 K, suggesting the presence of a tricritical point in the magnetic phase diagram of ErB_2 . Furthermore, when considering only magnetic field values above the spin-flip transition at 12 T, the magnetic phase diagram for field along the hard axis resembles strongly that for field along the easy axes.

IV. CONCLUSIONS

In summary, we reported an investigation of the low-temperature properties of single crystals of the hexagonal C32 diboride ErB_2 . Based on measurements of the magnetization, ac susceptibility, specific heat, and electrical resistivity, we find easy-plane ferromagnetic order below $T_c = 14$ K. Curie-Weiss fits to the ac susceptibility indicate ferromagnetic coupling along $\langle 100 \rangle$ and $\langle 210 \rangle$, antiferromagnetic coupling along $\langle 001 \rangle$, and fluctuating moments that are consistent with the free-ion value of Er^{3+} . However, a lack of saturation in the magnetization at high fields, typically attributed to itinerant magnetism, suggests that the 4f electrons may be hybridized with d electrons at the Fermi level.

A strong magnetic anisotropy dominates the magnetic properties at low temperatures, where the hexagonal basal plane is magnetically easy with a vanishingly small in-plane anisotropy and a magnetic hard $\langle 001 \rangle$ axis. For field within the basal plane, the magnetic properties are

reminiscent of a soft ferromagnet that is polarized in fields above a few tenth of a Tesla, while for field along (001) a spin-flip transition into the field-polarized state is observed at ~ 12 T. The magnetic anisotropy dominates the paramagnetic state up to $T_x = 50$ K, where magnetic fluctuations are essentially confined to the basal plane. As a function of magnetic field and temperature, crossover between the field-polarized, the paramagnetic, and the anisotropy-dominated regime may be distinguished featuring distinct changes in the spectrum of magnetic fluctuations.

Acknowledgments

We wish to thank A. Engelhardt, S. Mayr, W. Simeth, and M. Stekiel for fruitful discussions and assistance with

the experiments. This study was funded by the Deutsche Forschungsgemeinschaft (DFG, German Research Foundation) under TRR80 (From Electronic Correlations to Functionality, Project No. 107745057), TRR360 (Constrained Quantum Matter, Project No. 492547816), SPP2137 (Skyrmionics, Project No. 403191981, Grant PF393/19), and the excellence cluster MCQST under Germany's Excellence Strategy EXC-2111 (Project No. 390814868). Financial support by the European Research Council (ERC) through Advanced Grants No. 291079 (TOPFIT) and No. 788031 (ExQuiSid) is gratefully acknowledged.

-
- * Electronic address: c.resch@tum.de
- ¹ A. H. Silver and T. Kushida, *J. Chem. Phys.* **38**, 865 (1963).
 - ² R. G. Barnes and R. B. Creel, *Phys. Lett. A* **29**, 203 (1969).
 - ³ M. Kasaya and T. Hihara, *J. Phys. Soc. Jpn.* **29**, 336 (1970).
 - ⁴ T. Tanaka, H. Nozaki, E. Bannai, Y. Ishizawa, S. Kawai, and T. Yamane, *J. Less Common Met.* **50**, 15 (1976).
 - ⁵ S. Funahashi, Y. Hamaguchi, T. Tanaka, and E. Bannai, *Solid State Commun.* **23**, 859 (1977).
 - ⁶ V. A. Gasparov, N. S. Sidorov, I. I. Zver'kova, and M. P. Kulakov, *JETP Lett.* **73**, 532 (2001).
 - ⁷ H. Takeya, A. Matsumoto, K. Hirata, Y. S. Sung, and K. Togano, *Physica C* **412–414**, 111 (2004).
 - ⁸ C. A. Nunes, D. Kaczorowski, P. Rogl, M. R. Baldissera, P. A. Suzuki, G. C. Coelho, A. Grytsiv, G. André, F. Bouréé, and S. Okada, *Acta Mater.* **53**, 3679 (2005).
 - ⁹ Y. Singh, A. Niazi, M. D. Vannette, R. Prozorov, and D. C. Johnston, *Phys. Rev. B* **76**, 214510 (2007).
 - ¹⁰ B. J. Suh, X. Zong, Y. Singh, A. Niazi, and D. C. Johnston, *Phys. Rev. B* **76**, 144511 (2007).
 - ¹¹ N. L. Okamoto, M. Kusakari, K. Tanaka, H. Inui, and S. Otani, *Acta Mater.* **58**, 76 (2010).
 - ¹² A. Bauer, A. Regnat, C. G. F. Blum, S. Gottlieb-Schönmeyer, B. Pedersen, M. Meven, S. Wurmehl, J. Kuneš, and C. Pfleiderer, *Phys. Rev. B* **90**, 064414 (2014).
 - ¹³ J. Nagamatsu, N. Nakagawa, T. Muranaka, Y. Zenitani, and J. Akimitsu, *Nature* **410**, 63 (2001).
 - ¹⁴ J. Kortus, I. I. Mazin, K. D. Belashchenko, V. P. Antropov, and L. L. Boyer, *Phys. Rev. Lett.* **86**, 4656 (2001).
 - ¹⁵ H. J. Choi, D. Roundy, H. Sun, M. L. Cohen, and S. G. Louie, *Nature* **418**, 758 (2002).
 - ¹⁶ I. I. Mazin, O. K. Andersen, O. Jepsen, O. V. Dolgov, J. Kortus, A. A. Golubov, A. B. Kuz'menko, and D. van der Marel, *Phys. Rev. Lett.* **89**, 107002 (2002).
 - ¹⁷ K. H. J. Buschow, in *Boron and Refractory Borides*, edited by V. I. Matkovich (Springer, 1977), p. 494.
 - ¹⁸ G. Will and W. Schafer, *J. Less Common Met.* **67**, 31 (1979).
 - ¹⁹ M. A. Avila, S. L. Bud'ko, C. Petrovic, R. A. Ribeiro, P. C. Canfield, A. V. Tsvyashchenko, and L. N. Fomicheva, *J. Alloy Compd.* **358**, 56 (2003).
 - ²⁰ V. V. Novikov and A. V. Matovnikov, *J. Therm. Anal. Calorim.* **88**, 597 (2007).
 - ²¹ T. Mori, T. Takimoto, A. Leithe-Jasper, R. Cardoso-Gil, W. Schnelle, G. Auffermann, H. Rosner, and Y. Grin, *Phys. Rev. B* **79**, 104418 (2009).
 - ²² D. Bitko, T. F. Rosenbaum, and G. Aeppli, *Phys. Rev. Lett.* **77**, 940 (1996).
 - ²³ H. v. Löhneysen, A. Rosch, M. Vojta, and P. Wölfle, *Rev. Mod. Phys.* **79**, 1015 (2007), URL <https://link.aps.org/doi/10.1103/RevModPhys.79.1015>.
 - ²⁴ A. Wendl, H. Eisenlohr, F. Rucker, C. Duvinage, M. Kleinhans, M. Vojta, and C. Pfleiderer, *Nature* **609**, 65 (2022).
 - ²⁵ H. Chen, Q. Niu, and A. H. MacDonald, *Phys. Rev. Lett.* **112**, 017205 (2014).
 - ²⁶ S. Nakatsuji, N. Kiyohara, and T. Higo, *Nature* **527**, 212 (2015).
 - ²⁷ A. K. Nayak, J. E. Fischer, Y. Sun, B. Yan, J. Karel, A. C. Komarek, C. Shekhar, N. Kumar, W. Schnelle, J. Kübler, et al., *Sci. Adv.* **2**, e1501870 (2016).
 - ²⁸ A. M. Kosevich, B. A. Ivanov, and A. S. Kovalev, *Phys. Rep.* **194**, 117 (1990).
 - ²⁹ S. Artyukhin, M. Mostovoy, N. P. Jensen, D. Le, K. Prokes, V. G. de Paula, H. N. Bordallo, A. Maljuk, S. Landsgesell, H. Ryll, et al., *Nat. Mater.* **11**, 694 (2012).
 - ³⁰ J. B. Kargin, C. R. S. Haines, M. J. Coak, C. Liu, A. V. Matovnikov, V. V. Novikov, A. N. Vasiliev, and S. S. Saxena, in *2nd Int. Multidiscip. Microsc. Microanal. Congr.*, edited by E. Polychroniadis, A. Y. Oral, and M. Ozer (Springer International Publishing, 2015), p. 183.
 - ³¹ V. Novikov and T. Chukina, *Phys. Status Solidi B* **248**, 136 (2011).
 - ³² V. V. Novikov, T. A. Chukina, and A. A. Vervevkin, *Phys. Solid State* **52**, 364 (2010).
 - ³³ A. V. Matovnikov, V. S. Urbanovich, T. A. Chukina, A. A. Sidorov, and V. V. Novikov, *Inorg. Mater.* **45**, 366 (2009).
 - ³⁴ R. N. Castellano, *Mater. Res. Bull.* **7**, 261 (1972).
 - ³⁵ D. Nuzhina, Master's thesis (2023).
 - ³⁶ A. Tong, D. Nuzhina, C. Resch, G. Benka, A. Bauer, and C. Pfleiderer, (unpublished).

- ³⁷ A. Bauer, G. Benka, A. Neubauer, A. Regnat, A. Engelhardt, C. Resch, S. Wurmehl, C. G. F. Blum, T. Adams, A. Chacon, et al., *Phys. Status Solidi B* **259**, 2100159 (2022).
- ³⁸ G. Benka, Ph.D. thesis (2021).
- ³⁹ C. Resch, A. Bauer, M. Stekiel, F. Kübelbäck, J. Lass, G. Benka, L. Maximov, and C. Pfleiderer, (unpublished).
- ⁴⁰ A. Bauer, M. Garst, and C. Pfleiderer, *Phys. Rev. Lett.* **110**, 177207 (2013).
- ⁴¹ A. Aharoni, *J. Appl. Phys.* **83**, 3432 (1998).
- ⁴² A. Bauer and C. Pfleiderer, in *Topological Structures in Ferroic Materials: Domain Walls, Vortices and Skyrmions*, edited by J. Seidel (Springer, 2016), p. 1.
- ⁴³ A. P. Ramirez, *Annu. Rev. Mater. Sci.* **24**, 453 (1994).
- ⁴⁴ A. Bauer, G. Benka, A. Regnat, C. Franz, and C. Pfleiderer, *Rev. Sci. Instrum.* **87**, 113902 (2016).
- ⁴⁵ V. V. Novikov and A. V. Matovnikov, *Inorg. Mater.* **44**, 134 (2008).
- ⁴⁶ C. Thessieu, C. Pfleiderer, A. N. Stepanov, and J. Flouquet, *J. Phys.: Condens. Matter* **9**, 6677 (1997).
- ⁴⁷ A. Bauer, A. Neubauer, C. Franz, W. Münzer, M. Garst, and C. Pfleiderer, *Phys. Rev. B* **82**, 064404 (2010).
- ⁴⁸ A. Bauer, A. Senyshyn, R. Bozhanova, W. Simeth, C. Franz, S. Gottlieb-Schönmeyer, M. Meven, T. E. Schrader, and C. Pfleiderer, *Phys. Rev. Mater.* **6**, 034406 (2022).
- ⁴⁹ At low temperatures, typically $T < \Theta_D/10$, the Debye model yields a phonon contribution of the specific heat that scales with temperature to the power of three. At high temperatures, i.e., $T > \Theta_D$, the Debye model approaches the Dulong–Petit value. At intermediate temperatures, the Debye model provides a rough approximation of the phonon contribution to the specific heat that describes the situation in many materials surprisingly well. The deviations observed in the diborides do not permit to infer a Debye temperature from the low-temperature part of the Debye model using a linear fit to C/T as a function of T^2 for temperatures $T_c < T < \Theta_D/10$.